Fragmentation and solidification of fusible alloy melt by water spray

Hikita, Wataru
Department of Aeronautics and Astronautics, Kyushu University

Hirayama, Shodai
Department of Aeronautics and Astronautics, Kyushu University

Inoue, Chihiro
Department of Aeronautics and Astronautics, Kyushu University : Associate Professor

Wang, Zhenying
Department of Aeronautics and Astronautics, Kyushu University

他

出版情報：Powder Technology. 409, pp.117778-, 2022-07-06. Elsevier
バージョン：
権利関係：

Graphical Abstract

Fragmentation and solidification of fusible alloy melt by water spray

Wataru Hikita, Shodai Hirayama, Chihiro Inoue, Zhenying Wang, Makoto Nakaseko, Takuya Takashita

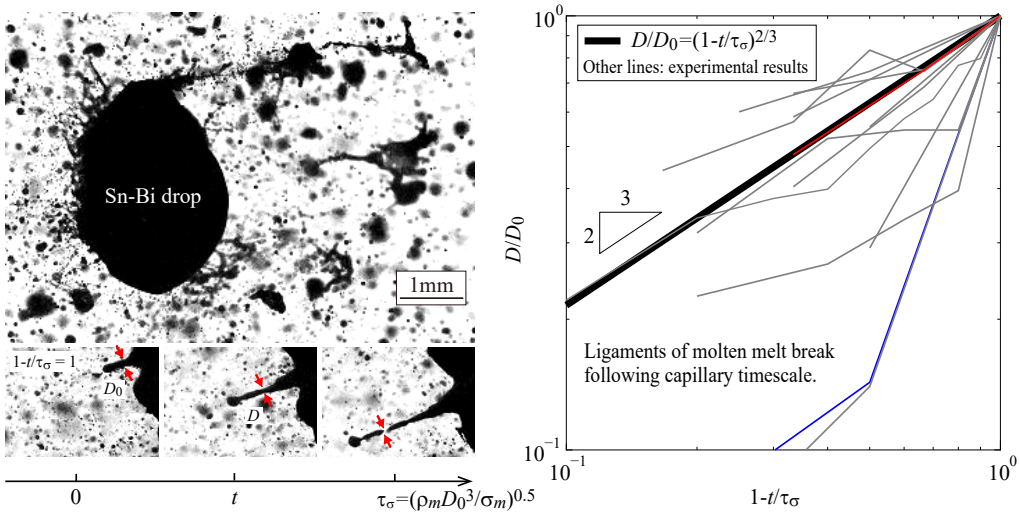

Highlights

Fragmentation and solidification of fusible alloy melt by water spray

Wataru Hikita, Shodai Hirayama, Chihiro Inoue, Zhenying Wang, Makoto Nakaseko, Takuya Takashita

- Successful visualization of disintegrating alloy ligaments inside a water spray
- Fragmentation follows capillary timescale with partial stretching by impinging water
- Non-uniform solidification of elongated drops creates particles with less circularity

Fragmentation and solidification of fusible alloy melt by water spray

Wataru Hikita[a], Shodai Hirayama[a], Chihiro Inoue[a], Zhenying Wang[a], Makoto Nakaseko[b], Takuya Takashita[b]

[a]*Department of Aeronautics and Astronautics, Kyushu University, 744 Motooka, Nishi-ku, Fukuoka, 819-0395, Japan*
[b]*JFE Steel, 1 Kawasaki-cho, Chuo-ku, Chiba, 260-0835, Japan*

Abstract

To elucidate from a thermo-fluid perspective the fragmentation and solidification processes that occur during the production of a metal powder, we conducted experiments to visualize the water atomization of molten 42Sn–58Bi fusible alloy and made measurements of the circularity of the resulting metal powder. The fragmentation process inside a fully developed fast water spray with a pressure up to 5 MPa was clearly captured. The time-resolved images revealed fragmentation patterns involving extending molten ligaments resulting from splashing, vapor explosions, and splitting. The time variation of the thinning of the neck diameter of the ligaments revealed that the fragmentation is rate-controlled by the capillarity of the molten drop itself, and solidification and viscosity have no influence on the pinching-point dynamics. The produced metal powder displayed size-dependent circularity, and larger particles tended to be less spherical than small particles. The mechanism is attributed to non-uniform solidification, which is enhanced at the pinching part of a droplet, consistent well with the images obtained.

Keywords: Liquid metal, Fusible alloy, Fragmentation, Capillarity, Solidification, Visualization

Nomenclature

a	Diameter of nozzle for molten alloy, m
C	Circularity
d	Drop diameter, m
D	Neck diameter, m
m	Mass of a water drop, kg
M	Mass of an alloy drop, kg
n	Number density in a unit area, m^{-2}
Nu	Nusselt number
$\dot{N}$	Frequency of impingement, s^{-1}
Oh	Ohnesorge number
P	Water injection pressure, Pa
Re	Reynolds number
S	Surface area, m^2
t	Time, s
T	Temperature, K
u	Velocity of alloy, m/s
V	Velocity of water spray, m/s
We	Weber number
x, y, z	Coordinates, m
$\langle X \rangle$	Mean value of X

Greek symbols

α	Thermal diffusivity, m^2/s
λ	Thermal conductivity, W/m·K
μ	Coefficient of viscosity, Pa·s
ν	Kinematic viscosity, m^2/s
ρ	Density, kg/m^3
σ	Surface tension coefficient, N/m
τ	Timescale, s
ξ	Normalized drop diameter ($d/\langle d \rangle$)

Subscripts

0	Initial value
m	Metal
α	Thermal diffusion
ν	Viscosity
σ	Capillarity

1. Introduction

Metal powders have applications in areas including sintering, welding, and metal injection molding [1–4], as well as additive manufacturing [5, 6], and demand for them is continuing to grow. It is thus desirable to produce large quantities of high-quality fine spherical particles with the lowest possible cost [7, 8]. Gas and water atomization techniques are widely applied to the production of metal powders. The large momentum of a inert gas jet or a fast water spray disintegrates the melt into droplets, which solidifies to become metal powder [6, 9]. Gas atomization can produce particles that are more spherical [1, 3, 10–13], while water atomization is more cost-effective [1, 3, 14–18].

Historically, research examining water atomization has been conducted for production of powders in materials engineering [19–26]. However, a good physical understanding of the process from thermo-fluid perspective is essential to enable the efficient production of higher-quality powders. However, there is as yet a lack of clarity regarding the specifics of the mechanisms involved in this process; the topological conversion from the initial molten metal to a fine metal powder involves heat transfer accompanied by the phase changes of boiling water drops on the molten metal and the solidification of the metal particles.

Recently, the pinch-off process of a metal jet was examined for the production of satellite-free metal drops, applicable to on-demand printing [27, 28]. Persson et al. [26] established the mechanism causing low circularity in the carbon steel particles produced by a V-jet-type water atomization; this was attributed to collision and coalescence between metal droplets, but the fragmentation and solidification processes were not directly visualized. Hikita et al. [29] successfully visualized the sequential water atomization process of a fusible alloy melt, leading to a physical model for predicting the powder size. They suggested that when fragmenting metal particles smaller than a certain threshold, typical metal-powder production processes are strongly affected by solidification, based on the balance between thermal diffusion and capillarity. In this work, however, the essential fragmentation process *inside* the water spray was not visible, which should be clarified to gain a more substantial understanding of the water atomization process. To the best of the present authors' knowledge, no sequential images of a disintegrating molten melt inside a water spray accompanied by fast water droplets have yet been obtained.

In light of the above, in the present study, we sought to understand exactly how a metal powder is produced by a water spray. To this end, we conducted time-resolved visualizations of a fusible alloy drop colliding with a fully developed water spray using a high-speed imaging with a high-frequency pulsed laser. The detailed fragmentation and solidification processes were quantitatively clarified by Lagrangian tracking measurements, leading to the proposal of a mechanism determining the circularity of the resulting powder.

The remainder of this paper is structured as follows. The experimental methods are explained in Section 2, the results and discussion are presented in Section 3, and conclusions are summarized in Section 4.

2. Experimental Method

Fig. 1 illustrates the experimental apparatus, which consists of a single water spray spreading horizontally and a nozzle dropping molten fusible alloy perpendicularly onto this water spray. We define the origin of the coordinate system at the center of the water-nozzle exit, and the x, y, and z axes point in the horizontal direction, the water-spray width direction, and the vertical direction, respectively. In this system, the water spray is pressurized by a

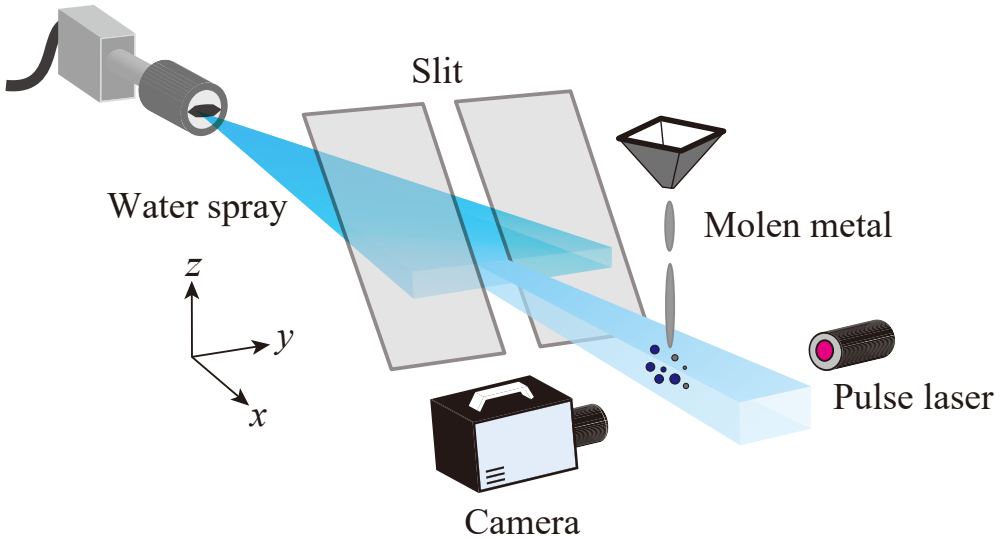

Figure 1: Experimental setup. The center of the water spray passes through a slit of 20 mm width between two metal plates.

pump (Kärcher HD 13/15 S) and ejected from a nozzle (Kärcher nozzle tip 15° 055) into still air. The two plates are set at $x = 400$ mm to reduce the width of the water spray, which is 20 mm in the y direction, so that closeup observations of the fragmenting fusible alloy inside the water spray can be made. Since the fusible alloy melt collides with center of the water spray, the plates do not affect the fragmentation events.

High-speed visualizations were conducted at $x = 700$ mm. We used a high-frequency pulsed laser (Cavitar CAVILUX Smart) as a back-lighting source, and this was synchronized to the exposure of a high-speed camera (Photron FASTCAM SA-Z) with a resolution of 1024×1024 pixels at a framerate of 20 kHz. The attached lens was a Micro-Nikkor 105 mm. For the close-up visualization of the fragmenting molten drops, the working distance to the plane of $y = 0$ mm was approximately 100 mm, and the typical depth of field was 2 mm. The water spray, which was moving at 100 m/s, traveled 3 μm in a single image illuminated by a short flashing pulse of 30 ns, and this was well captured by the unit pixel resolution of 20 μm. An image analyzer (Morphologi G3, Malvern Panalytical) was used to measure the circularity of the metal powders that were produced, as well as their diameter distributions, as described in our previous report [29]. Lens magnifications were 2.5x and 10x, and area-equivalent particle diameters were $3.5 \leq d \leq 1,000$ μm with the typical resolution of 0.5 μm.

The fusible alloy 42Sn–58Bi was used as the molten metal. As shown in Table 1, the melting point of this alloy is $T_\mathrm{m} = 412$ K, which is much lower

Table 1: Properties of fusible alloy 42Sn–58Bi.

Melting point	T_m	412 K
Density	ρ_m	8.7×10^3 kg/m^3
Surface tension coeff.	σ_m	0.5 N/m
Kinematic viscosity	ν_m	1.6×10^{-7} m^2/s
Thermal diffusivity	α_m	4.2×10^{-5} m^2/s

Table 2: Experimental conditions.

Water injection pressure	P	3 or 5 MPa
Liquid metal temperature	T_0	520 K
Nozzle diameter for metal	a	1 or 2 mm

than the melting point of practical metals used in industrial water atomization, e.g., stainless steel, which has a melting point of over 1500 K. The fragmentation process, however, is consistent, because the momentum of the water spray is still dominant when compared to the momentum of the molten metal. Moreover, the ratio of the capillary timescale $(\rho_{\mathrm{m}} d^3/\sigma_{\mathrm{m}})^{0.5}$ to the viscous timescale of d^2/ν_{m}—the so-called Ohnesorge number—is much less than unity for a particle size of $d \sim 10^{-4}$ m; thus, the effects of viscosity on the metal-fragmentation process are negligible (see Appendix A). At room temperature, the water spray has a density of $\rho = 10^3$ kg/m^3, a surface tension coefficient of $\sigma = 0.07$ N/m, and a kinematic viscosity of $\nu = 10^{-5}$ m^2/s.

The experimental conditions are summarized in Table 2. The total pressure of the water spray was $P = 3$ or 5 MPa. After the water spray had fully developed, the fusible alloy melt—which was heated to $T = 520$ K by a mantle heater—was freely dropped toward the $-z$ direction from the nozzle, which was located $z = 150$ mm above the spray. Two diameters were used for the nozzle: $a = 1$ and 2 mm.

3. Results and discussion

We first present an overview of the water sprays and their velocity and size distributions. This is followed by the presentation of sequential fragmentation images of the fusible alloy melt inside the water spray and a description of the solidification process determining the circularity of the resulting powder.

3.1. Water spray

Fig. 2 shows images of the water spray in the x–y and z–x planes, as well as velocity distributions along the centerline in the x–y plane in the absence of the fusible alloy. At $P = 3$ MPa, a flat fan-type spray develops with an apex angle of 20° in the x–y plane, and this disintegrates into ligaments and droplets. In the z–x plane, the spray thickens to 10 mm in the z direction. We manually conducted particle-tracking velocimetry using the ImageJ software package [30], measuring the displacements of ten specified ligaments or droplets between two frames at an axial position. The mean axial velocity of the water spray along the centerline was $V \approx 50$ m/s. At $P = 5$ MPa, the spray velocity increased to $V \approx 80$ m/s, but the overall spray structure, including the apex angle and thickness, coincided with the case at $P = 3$ MPa. As the spray develops, the axial velocity gradually decreases downstream due to aerodynamic drag.

At $x = 700$ mm, the diameters, d, of over 50,000 particles were measured as the area-equivalent diameter by using ImageJ [30]. The size distribution of $\xi = d/\langle d \rangle$, depicted as probability density function (PDF) for a fully

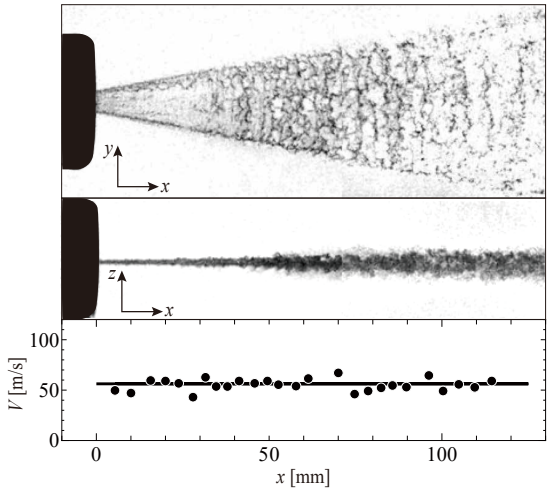

(a) $P = 3$ MPa.

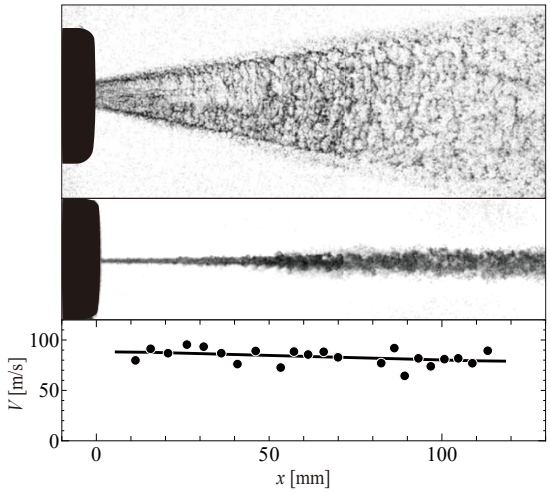

(b) $P = 5$ MPa.

Figure 2: Snapshots the of water spray and plots of its axial velocity distribution. The spray velocity was measured along the centerline in the x–y plane.

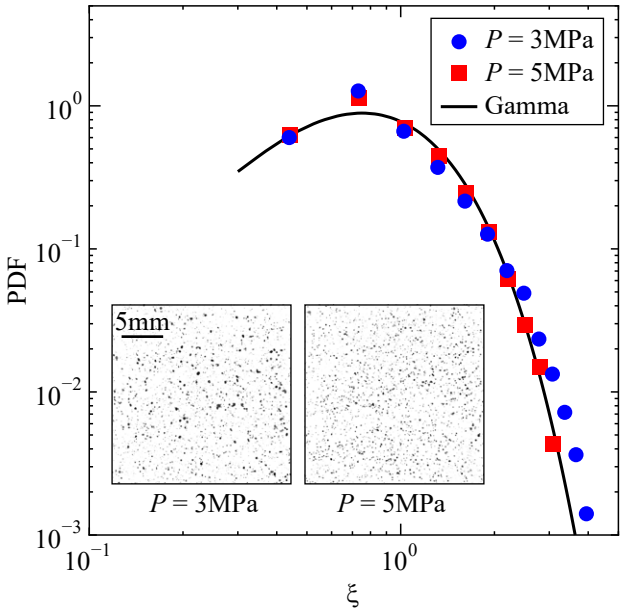

Figure 3: Water droplet diameter distributions with the spray images at $x = 700$ mm. Here, the two plates are installed at at $x = 400$ mm.

developed spray obeys a unique Gamma distribution[31, 32].

$$\mathrm{PDF}(\xi) = \frac{k^k}{\Gamma(k)} \xi^{k-1} e^{-k\xi}. \tag{1}$$

In the present experiment, the mean diameter was $\langle d \rangle \approx 0.10$ mm in both cases of $P = 3$ and 5 MPa. Fig. 3 shows that the PDFs for small drops in the range $\xi \leq 2$ are independent of the water injection pressure; however, for $P = 5$ MPa, large drops of $\xi > 2$ are slightly less common than for $P = 3$ MPa. We confirm that the overall trend of the PDF as a function of ξ follows the Gamma distribution with $k = 4$. This provides evidence that the water spray is fully discretized at this position, as can also be deduced qualitatively from the spray images. The two plates set upstream at $x = 400$ mm demonstrate no essential effects to the water spray characteristics.

For a water spray of $P = 3$ or 5 MPa, at $x = 700$ mm, the water drop velocity decreases to $V \approx 30$ m/s. A denser spray is produced at $P = 5$ MPa than at $P = 3$ MPa, while the number density is consistently $n \approx 5$ mm^{-2}. The rate of impingement of the water spray on the molten metal dropped from a nozzle of diameter $a \sim O(10^{-3})$ m is estimated as $\dot{N} \approx naV \sim 10^5$ s^{-1}.

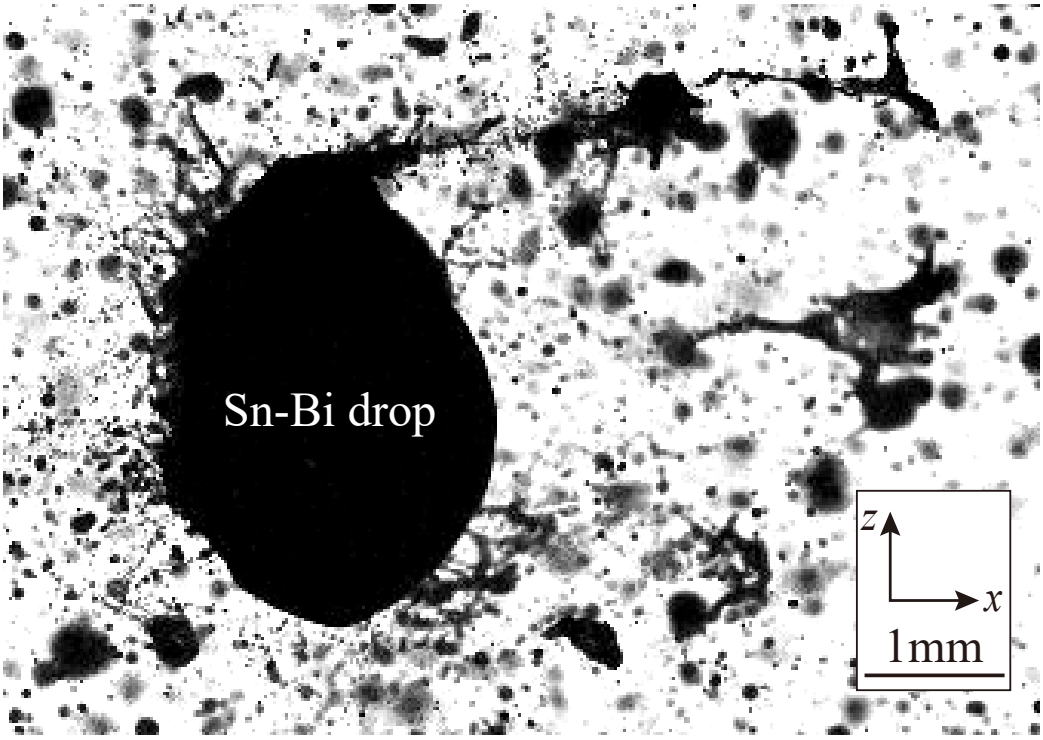

Figure 4: A fusible alloy drop being fragmented by impinging water droplets at $P = 3$ MPa in the z–x plane.

3.2. Fragmentation of fusible alloy melt

Fig. 4 shows an instantaneous image of a fragmenting fusible alloy melt drop released from a nozzle of $a = 1$ mm inside the water spray at $x = 700$ mm. Rapidly spreading water droplets impact on the alloy drop's upstream surface, producing ligaments of the fusible alloy melt [33, 34]. Simultaneously, the large-momentum water droplets split the upper edge of the molten drop producing a stretched ligament. Conversely, the downstream surface remains smooth without the impingement of the water spray. Consistently, most of the fragmentation process is completed in a single event by ligament breakup rather than through the impingement of multiple successive water droplets [35].

Fig. 5 presents time-series visualization results of fragmenting fusible alloy melt at $a = 1$ mm. At $P = 3$ MPa, the falling fusible alloy collides with the spreading water droplets, moving in the positive x direction. The deformation of the fusible alloy is not significant. At $P = 5$ MPa, the fusible

alloy is strongly distorted by the impingement of fast water droplets, which leads to fragmentation of small alloy droplets from the top and bottom sides during $t = 1$–3 ms. It is evident that the large momentum of the water spray splits the alloy droplets, and this is the primary mechanism of metal powder generation. During $t = 4$–7 ms, the remaining fusible alloy deforms as it moves downstream. The timescale for water droplets passing the fusible alloy is $a/V \sim O(10^{-4})$ s, much shorter than the visualization time of $O(10^{-2})$ s in Fig. 5. This indicates that the fragmentation of the alloy proceeds not instantaneously but gradually, originating from the alloy's surface by direct impingement of water droplets.

In Fig. 5, for a molten drop with mass $M \propto \rho_{\mathrm{m}} a^3$, the increase of velocity along the x direction is $\Delta u \sim 1$ m/s in the period $\Delta t \sim 10$ ms. Assuming that the inertia of a single water droplet with the mean mass of $\langle m \rangle \propto \rho \langle d \rangle^3$ is fully converted to the momentum change of the molten metal at the impinging

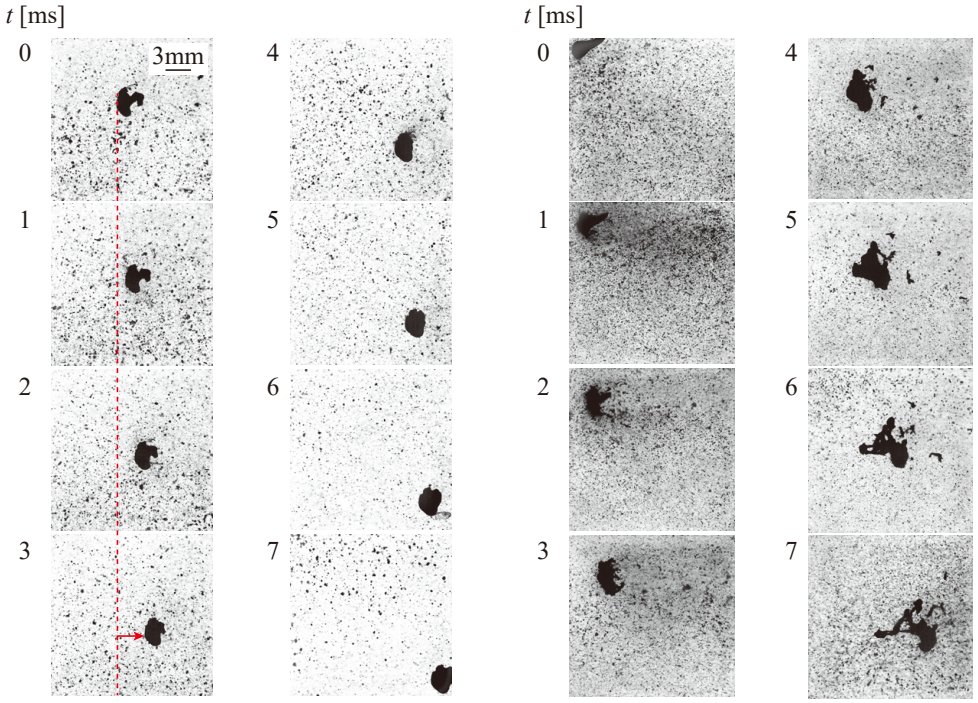

(a) $P = 3$ MPa. (b) $P = 5$ MPa.

Figure 5: Time-variant fragmentation process at $a = 1$ mm in the z–x plane.

frequency of $\dot{N}$ in the x direction, the momentum conservation between the molten drop and water droplets is deduced as:

$$\dot{N}\Delta t\langle m\rangle V \approx M\Delta u. \tag{2}$$

We find that the rate of impingement of water droplets is $\dot{N} \sim 10^5$ s^{-1}, and this is consistent with the measurements of the water spray in Fig. 3. Throughout the fragmentation and deformation of the molten drop, the increase in the surface area is ΔS, as obtained by energy conservation:

$$\dot{N}\Delta t\frac{1}{2}\langle m\rangle V^2 \sim \sigma_{\mathrm{m}}\Delta S. \tag{3}$$

Here, the change in the kinematic energy of the molten drop is negligible. During the period $\Delta t \sim 10$ ms in Fig. 5, we can deduce $\Delta S \sim 10^{-5}$ m^2; the surface area rapidly becomes ten times greater than the original surface area as a result of colliding with the water spray.

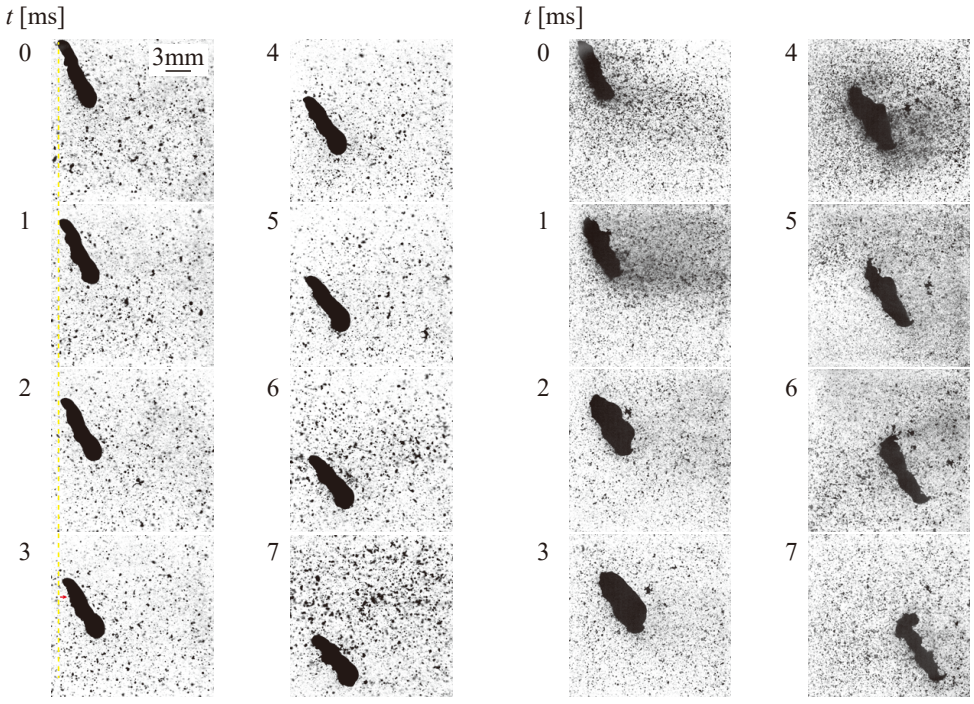

(a) $P = 3$ MPa. (b) $P = 5$ MPa.

Figure 6: Time-variant fragmentation process at $a = 2$ mm in the z–x plane.

Fig. 6 shows the fragmentation process at $a = 2$ mm. The shape of the fusible alloy is a column rather than a sphere, as observed at $a = 1$ mm. At $P = 3$ MPa, the larger mass of the molten column restricts its horizontal

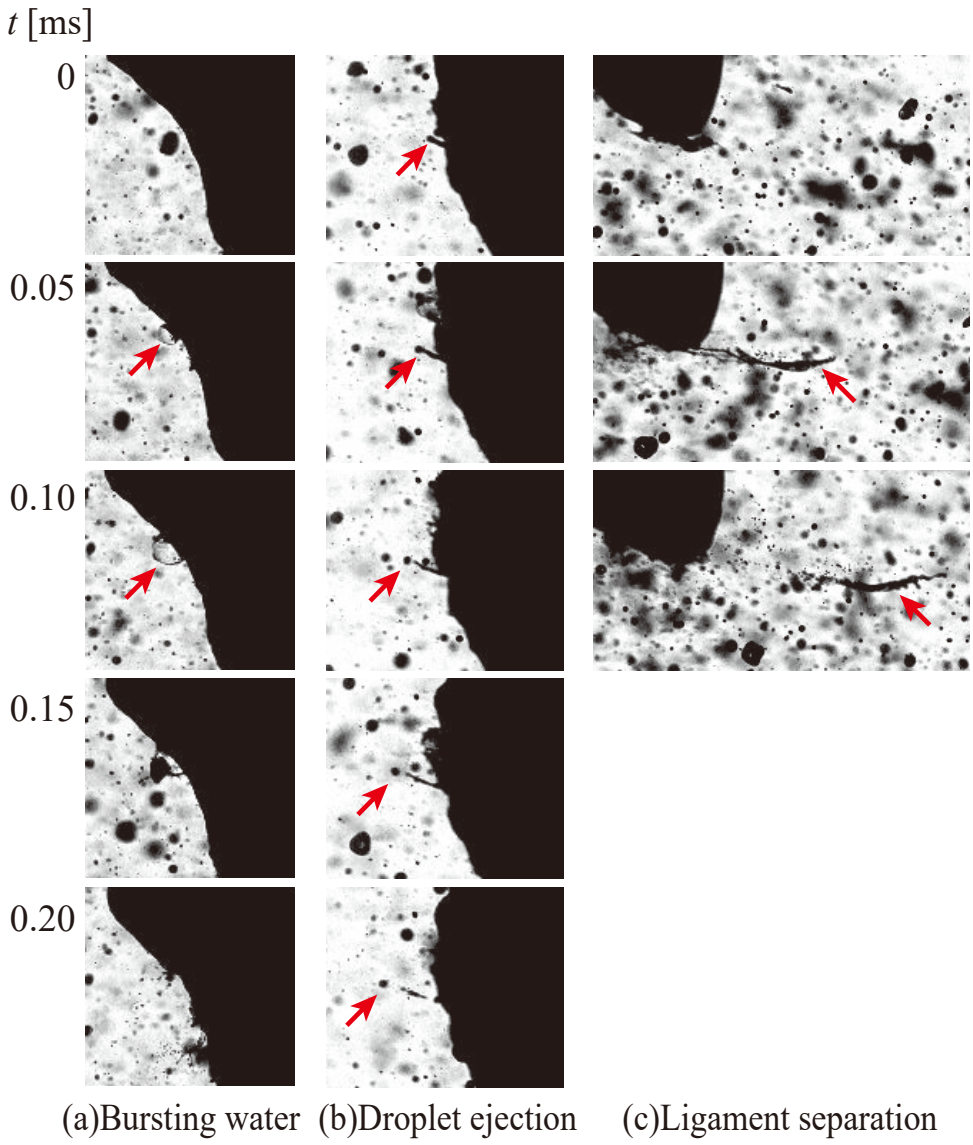

Figure 7: Typical events during water atomization in the z–x plane.

displacement when compared with Fig. 5(a). The column rotates in the anti-clockwise direction because the bottom of the column penetrates the water spray first. At $P = 5$ MPa, we can clearly confirm fragmentation from the fusible column surface and deformation of the column body. Visible topological changes in the fusible alloy melts suggest that they are in the liquid phase, and this is consistent for both $a = 1$ and 2 mm.

Magnified images are shown in Fig. 7. In Fig. 7(a), a water droplet adhering to the surface of the hot alloy nucleates and bursts, forming a transparent bubble. When a water droplet penetrates into the upstream surface of the alloy, the water is heated by the surrounding melt to a temperature exceeding 373 K. The rapid vaporization causes a bursting bubble to form, leading to ligament ejection and droplet disintegration [36] in the upstream direction (the opposite of the water spray direction), as shown in Fig. 7(b). This was also confirmed in a previous report [29]. In Fig. 7(c), large-momentum water droplets impinging on the rim of the alloy melt split the ligament downstream, and this becomes separated from the melt body.

Since all the metal droplets are produced through ligaments, we tracked a neck or constriction point on a ligament to measure its time-variant diameter D in the z–x plane. As shown in Fig. 8(a), the initial diameter of $D = D_0$ is visible at $t = 0$ s, and the neck becomes thinner until $D = 0$ at $t = \tau_\sigma$. Assuming that the disintegration of the metal ligament is rate-controlled by capillarity in the liquid phase, we deduce $\tau_\sigma \sim (\rho_\mathrm{m} D_0^3/\sigma_\mathrm{m})^{0.5}$ or $\tau_\sigma - t \sim (\rho_\mathrm{m} D^3/\sigma_\mathrm{m})^{0.5}$, in which $D = D_0$ at $t = 0$ and $D = 0$ at $t = \tau_\sigma$. The pinching of the normalized neck diameter obeys the equation:

$$\frac{D}{D_0} \sim \left(1 - \frac{t}{\tau_\sigma}\right)^{\frac{2}{3}}. \tag{4}$$

In Fig. 8(b), it can be seen that most of the measured neck diameter thins following Eq. (4). This provides evidence that the neck-pinching process is dominated by capillarity in the liquid phase, there are no effects from solidification, and the surface tension coefficient is constant. Some ligaments shrink more rapidly than the capillary timescale, indicating that stretching by the impingement of the fast water spray partially affects their extension. The moment of pinching, however, is dominated by capillarity. When the inertia of a ligament overcomes the capillary force, it extends with velocity

u, following $We = \rho_m u^2 D_0/\sigma_m \sim O(10^1)$, corresponding with:

$$u \sim \sqrt{\frac{\sigma_m}{\rho_m D_0}}. \tag{5}$$

We confirm in Fig. 8(c) that the ligaments produced by splashing water

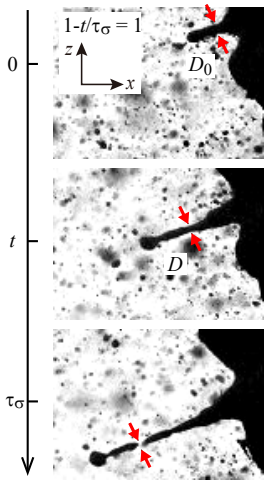

(a) Extending ligament.

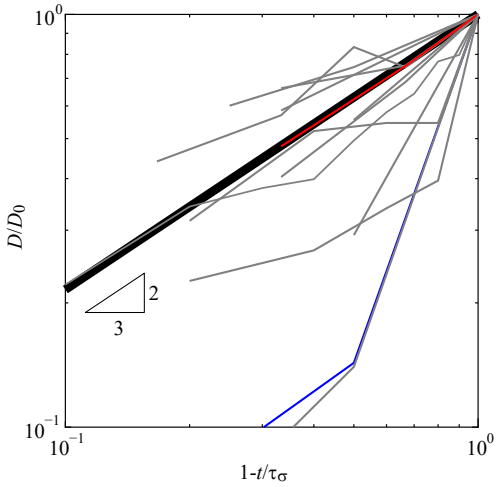

(b) Time-variant neck diameter.

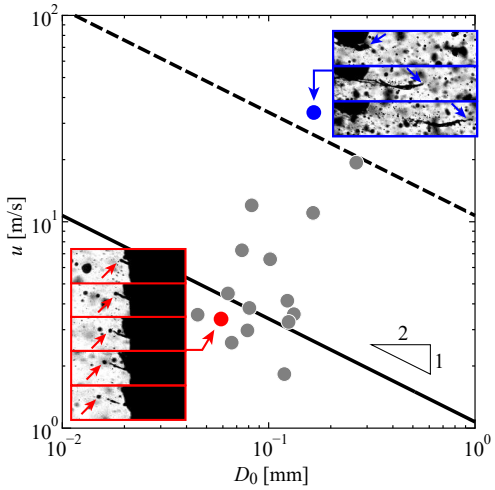

(c) Ligament extension velocity.

Figure 8: Experimental results of ligament dynamics. The bold line in (b) follows the capillary timescale. The solid and dashed lines in (c) indicate $We = 10$ and $We = 1000$, respectively. Blue and red circles correspond to lines of the same color in (b).

droplets and water-vapor explosion extend following $We \sim O(10^1)$. Ligaments split by the fast water droplets on the rim of the molten drop extend rapidly as $We \gg O(10^1)$, having approximately the same spreading velocity as the water droplets.

The above discussion convinces us that the fragmentation process of a molten drop by a fast water spray is a capillary-dominant phenomenon, wherein the viscosity and solidification are both insignificant to the final pinching point.

3.3. Solidification and circularity

Molten droplets fragmenting through ligament breakup in the liquid phase eventually solidify to become metal particles. We measured the circularity of the powder produced by a water spray at $P = 5$ MPa at the collision point of $x = 100$ mm, and the results are shown in Fig. 9. The experimental results plotted for 50,000 particles depicted by the gray cross marks in Fig. 9(a) show that the circularity varies widely for small particles of $d \leq 50$ μm, and it converges to become constant for large particles of $d \geq 100$ μm. The mean circularity $\langle C \rangle$ is, however, high for small particles and low for large ones, such that $\langle C \rangle \approx 0.9$ at $d = 10$ μm and $\langle C \rangle \approx 0.7$ at $d = 100$ μm. This trend is consistent with the recent results of Persson et al. [26], in which larger

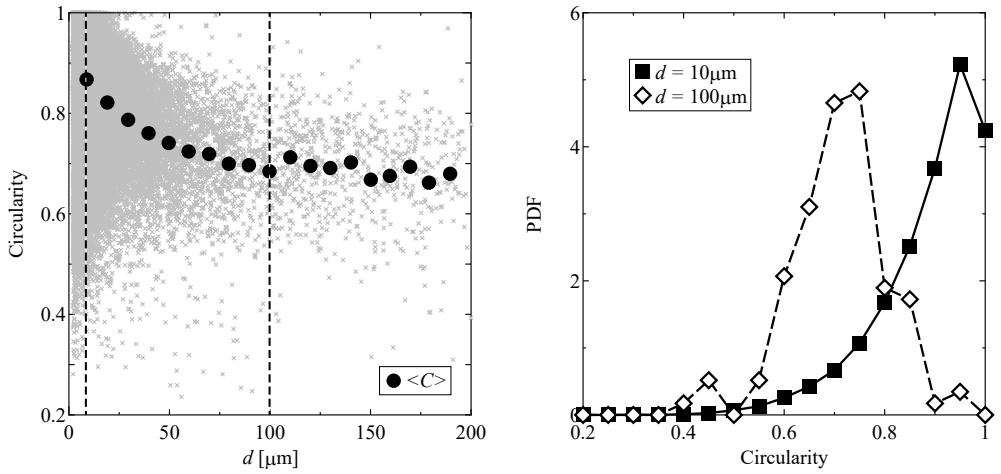

(a) Circularity and its mean values.

(b) PDF at $d = 10$ and 100 μm

Figure 9: Experimental results of circularity at $P = 5$ MPa. These experiments were conducted at an impinging point of $x = 100$ mm.

particles were found to be less spherical.

Fig. 9(b) shows the PDFs of the circularity at $d = 10$ and 100 μm along the dashed lines in Fig. 9(a). We can quantitatively confirm that high-circularity particles are more frequent at $d = 10$ μm than at $d = 100$ μm. The fact that small particles are highly circular is counter to the idea that larger particles will have more time to become spherical in the liquid phase; specifically, the time available to become spherical is proportional to $d^{1.5}$, following the capillary timescale, and the time to freeze is approximately proportional to d^2, obeying the thermal-diffusion timescale (see Appendix B). This idea, however, hypothesizes that the solidifying particles will experience uniform solidification.

Fig. 10 reveals the size-dependent nature of the fragmentation and solidification processes. During $0.1 \leq t \leq 0.4$ ms, the small spherical droplet indicated by the blue arrow is pinched from the ligament tip, becoming spherical in $0.1 \leq t \leq 0.2$ ms as a result of the surface tension of the molten drop itself. Following larger droplets depicted by the green and red arrows in $0.6 \leq t \leq 3.0$ ms reveals that they are not spherical. Focusing on the last

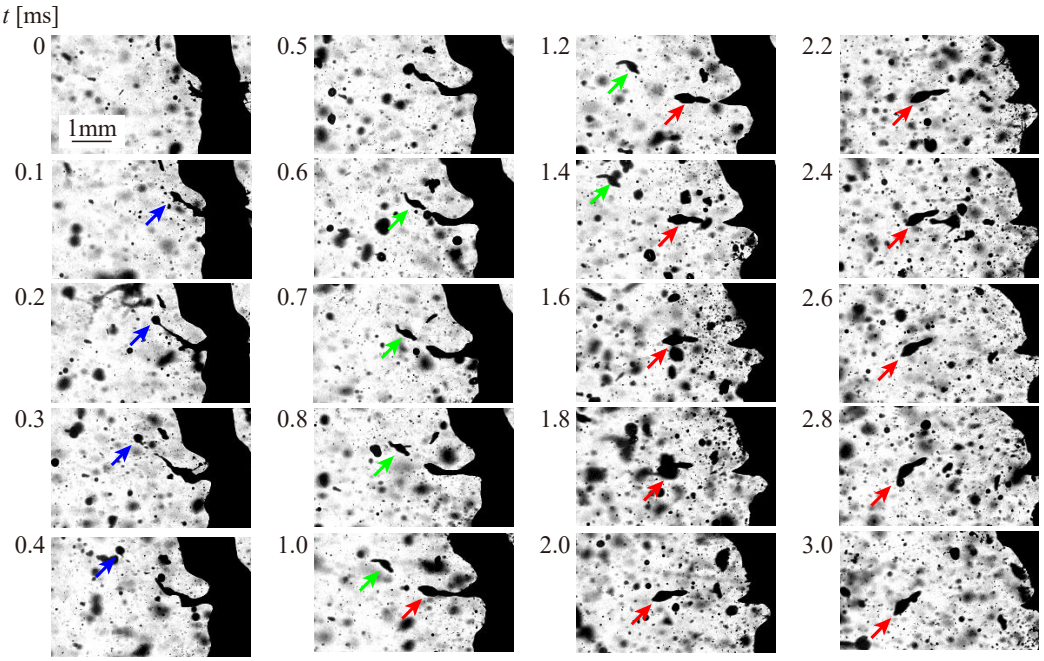

Figure 10: Typologies of pinched droplets in the z–x plane.

drop in the period $1.0 \leq t \leq 3.0$ ms, we can confirm that the shape does not change from its non-spherical topology, and it is identical to the disintegrating ligament at $t = 1.0$ ms.

Throughout the present visualization experiments, which have a spatial resolution of 20 μm/pix, we did not encounter any coalescence events of molten droplets after they had fragmented from the mother molten drop; this is consistent in Figs. 5 and 6, wherein the dense fragments near the mother molten drop spread to become sparse downstream, and coalescence rarely occurs. Previous scanning electron microscope images have revealed that small particles of $d \leq 10$ μm can coalesce with a large particle [26, 37] in a region of dense fragments, partially decreasing its circularity.

Based on the direct visual evidence, we propose a simple solidification model, as shown in Fig. 11. This is distinct from the mechanism based on coalescence of molten drops proposed by Persson et al. [26]. When a droplet that was originally a part of a columnar ligament disintegrates, the pinching points at the top and bottom parts in the illustration consistently have large curvature, and the strong surface tension in these regions causes the distorted tips to become hemispherical. Deformation of the pinching point soon ceases because this part is thin and solidification thus proceeds rapidly. Ultimately, the sphericalization cannot fully complete. The thick central body takes longer to solidify, in which the surface tension is weak due

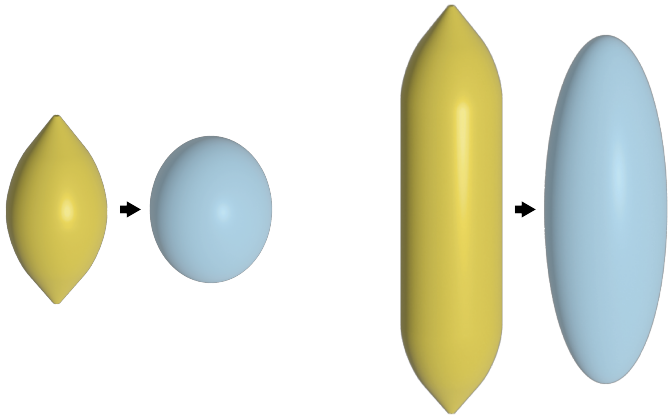

Figure 11: Solidification model. Solidifying short (left) and long (right) molten drops are shown after pinch-off from a ligament. Green shows the liquid phase, and blue indicates the solid phase.

to its small curvature. As a result, the shape of the droplet changes slightly at the pinched point. A short molten drop (Fig. 11, left) will thus tend to become more spherical and will have high circularity; in contrast, a long molten drop (Fig. 11, right) will remain elongated and have lower circularity.

Let us measure the representative drop size in Fig. 10 as $d \sim 10^{-4}$ m and assume that the neck diameter is one-tenth of this, $d_\mathrm{n} \sim 10^{-5}$ m. We can then compare the timescales for solidification and sphericalization, as previously analyzed by Nichiporenko [38] (see Appendix B). We estimate that the overall solidification time of $\tau_\alpha \sim d^2/\alpha_\mathrm{m} \sim 10^{-3}$ s, wherein the sensible heat becoming T_m and the latent heat of fusion are comparable, is longer than the time required to form a sphere in $\tau_\sigma \approx (\rho_\mathrm{m} d^3/\sigma_\mathrm{m})^{0.5} \sim 10^{-4}$ s. This indicates that the drops will become spherical, but this is inconsistent with the visual evidence in the period $1.0 \leq t \leq 3.0$ ms in Fig. 10. The pinching point can quickly solidify in a timescale of $\tau_\alpha \sim 10^{-5}$ s, which is equivalent to the local τ_σ, and this proceeds prior to overall solidification and sphericalization. The size-dependent circularity is thus the result of a mechanism whereby solidification occurs non-uniformly in the molten drops, progressing more quickly in thin areas.

4. Conclusion

We successfully conducted direct-visualization experiments to observe the fragmentation and solidification processes of molten 42Sn–58Bi fusible alloy inside a water spray with a pressure up to 5 MPa using high-frequency light pulses. From images of the impingement of fast water droplets on a falling molten drop, we confirmed that splashing and water-vapor explosions on the upstream molten surface and splitting of parts of the droplet's rim all produce extending ligaments. The fragmentation proceeds following the capillary timescale of the molten drop and is unaffected by solidification and viscosity. Measurement of the collected particles demonstrated size-dependent circularity: small particles are more spherical and large particles are irregular. This can be attributed to the non-uniform solidification of molten drop fragments. Surface tension, as the driving force leading to sphericality, works strongly at the pinching point; however, this thin part quickly freezes, meaning that long particles solidify with topology similar to that at their fragmenting moment, resulting in them having lower circularity.

Acknowledgement

This study was supported by JSPS KAKENHI (Grant Nos. JP21H01251 and JP22K18771).

Appendix A

Previous research has proposed timescales for a metal droplet to become spherical. Let us use the values listed in Table 2 and a droplet diameter of $d \sim 10^{-4}$ m. The coefficient of viscosity of the metal is given by $\eta_\mathrm{m} = \rho_\mathrm{m}\nu_\mathrm{m} = 1.4$ mPa·s. Nichiporenko [38] proposed viscous-capillarity timescale for the spheronization:

$$\tau_{\sigma\nu} \sim \frac{\eta_\mathrm{m} d}{\sigma} \sim O(10^{-7}) \text{ s}. \tag{6}$$

Yule and Dunkley [2] argued that Eq. (6) results in a significant underestimation, and they provided a viscous timescale:

$$\tau_\nu \sim \frac{d^2}{\nu_\mathrm{m}} \sim O(10^{-1}) \text{ s}. \tag{7}$$

As shown in Fig. 10 ($0.1 \leq t \leq 0.4$ ms), we confirmed that the time to become spherical follows the capillary timescale of $\tau_\sigma \approx (\rho_\mathrm{m} d^3/\sigma_\mathrm{m})^{0.5} \sim O(10^{-4})$ s. This fact is consistent with the Ohnesorge number being much less than unity, as $Oh = \tau_\sigma/\tau_\nu \sim O(10^{-3}) \ll 1$. In the present study, the viscosity was found to have no influence on the fragmentation and spheronization of the molten fusible alloy.

Appendix B

In the case of a small Biot number, the time taken for a spherical particle to cool down to the melting temperature can be deduced by solving an equation for heat transfer [38]:

$$\tau_\alpha = \frac{1}{6Nu}\frac{\lambda_\mathrm{m}}{\lambda}\frac{d^2}{\alpha_\mathrm{m}} \ln\frac{T_0 - T_\infty}{T_\mathrm{m} - T_\infty}. \tag{8}$$

At a Reynolds number of $Re = (V-u)d/\nu \sim O(10^2)$, we estimate the Nusselt number is $Nu \sim O(10^1)$. By using $\lambda_\mathrm{m}/\lambda \sim O(10^3)$ and $\ln\frac{T_0-T_\infty}{T_\mathrm{m}-T_\infty} \sim O(10^{-1})$

at $T_\infty = 300$ K, Eq. (8) can be simplified to $\tau_\alpha \sim d^2/\alpha_\mathrm{m}$ for the present experimental conditions. The visualization results in Fig. 10 show that the molten drops are cooled down by ambient air and possibly steam, whose values of thermal conductivity are similar ($\lambda \sim 10^{-2}$ W/m·K). τ_α can become shorter as a result of boiling heat transfer [38].

Declaration of Competing Interest

The authors declare no conflict of interest.

Author contributions

W.H.: Methodology, Data Curation, Investigation. S.H.: Data Curation. C.I.: Supervision, Conceptualization, Investigation, Writing – Review & Editing. Z.W.: Writing – Review & Editing. M.N.: Conceptualization, Resources. T.T.: Resources.

References

[1] R. M. German, Powder metallurgy science, Metal Powder Industries Federation, 105 College Rd. E, Princeton, N. J. 08540, U. S. A, 1984. 279 (1984).

[2] A. J. Yule, J. J. Dunkley, Atomization of melts: for powder production and spray deposition, no. 11, Oxford University Press, USA, 1994.

[3] R. M. German, Powder metallurgy and particulate materials processing: the processes, materials, products, properties and applications, Metal powder industries federation Princeton, 2005.

[4] D. F. Heaney, Handbook of metal injection molding, Woodhead Publishing, 2018.

[5] H. Kissel, Titanium powder and additive manufacturing: The perfect match, Metal Powder Report 76 (4) (2021) 196–198. doi:10.1016/j.mprp.2021.06.002.

[6] P. Moghimian, T. Poirié, K. M. Habibnejad, J. A. Zavala, J. Kroeger, F. Marion, F. Larouche, Metal powders in additive manufacturing: A review on reusability and recyclability of common titanium, nickel and

aluminum alloys, Additive Manufacturing 43 (2021) 102017. doi:10.1016/j.addma.2021.102017.

[7] S. Motaman, A. M. Mullis, R. F. Cochrane, D. J. Borman, Numerical and experimental investigations of the effect of melt delivery nozzle design on the open-to closed-wake transition in closed-coupled gas atomization, Metallurgical and Materials Transactions B 46 (4) (2015) 1990–2004. doi:10.1007/s11663-015-0346-6.

[8] G. Baudana, S. Biamino, D. Ugues, M. Lombardi, P. Fino, M. Pavese, C. Badini, Titanium aluminides for aerospace and automotive applications processed by electron beam melting: Contribution of politecnico di torino, Metal Powder Report 71 (3) (2016) 193–199. doi:10.1016/j.mprp.2016.02.058.

[9] P. Sun, Z. Z. Fang, Y. Zhang, Y. Xia, Review of the methods for production of spherical ti and ti alloy powder, JOM 69 (10) (2017) 1853–1860. doi:10.1007/s11837-017-2513-5.

[10] T. Kato, K. Kusaka, On the recent development in production technology of alloy powders, Materials Transactions, JIM 31 (5) (1990) 363–374. doi:10.2320/matertrans1989.31.363.

[11] L. Salgado, F. F. Ambrózio, M. Das Neves, E. Pola, O. De Souza, Characterization of ni-cu alloy powders produced by the atomization process, Materials Science and Engineering: A 133 (1991) 692–697. doi:10.1016/0921-5093(91)90164-I.

[12] H. Arachchilage, K, M. Haghshenas, S. Park, L. Zhou, Y. Sohn, B. McWilliams, K. Cho, R. Kumar, Numerical simulation of high-pressure gas atomization of two-phase flow: Effect of gas pressure on droplet size distribution, Advanced Powder Technology 30 (11) (2019) 2726–2732. doi:10.1016/j.apt.2019.08.019.

[13] W. S. Prashanth, S. L. Thotarath, S. Sarkar, T. N. C. Anand, S. Bakshi, Experimental investigation on the effect of melt delivery tube position on liquid metal atomization, Advanced Powder Technology 32 (3) (2021) 693–701. doi:10.1016/j.apt.2021.01.017.

[14] A.C.Reardon, Metallurgy for the Non-Metallurgist, Second Edition, ASM International, 2011.

[15] Y. Liu, S. Niu, F. Li, Y. Zhu, Y. He, Preparation of amorphous fe-based magnetic powder by water atomization, Powder technology 213 (1-3) (2011) 36–40. doi:10.1016/j.powtec.2011.06.026.

[16] A. R. Farinha, M. T. Vieira, R. Mendes, Explosive consolidation of 316l stainless steel powder–effect of phase composition, Advanced Powder Technology 25 (5) (2014) 1469–1473. doi:10.1016/j.apt.2014.08.012.

[17] M. Hebda, S. Gądek, K. Miernik, J. Kazior, Effect of the cooling rate on the phase transformation of astaloy crl powders modified with sic addition, Advanced Powder Technology 25 (2) (2014) 543–550. doi:10.1016/j.apt.2013.09.001.

[18] S. Cacace, Q. Semeraro, Influence of the atomization medium on the properties of stainless steel slm parts, Additive Manufacturing 36 (2020) 101509. doi:10.1016/j.addma.2020.101509.

[19] A. T. Ankus, R. D. Venter, The water atomization of silver: Effect of pressure and superheat, Powder Technology 73 (2) (1992) 169–179. doi:10.1016/0032-5910(92)80078-B.

[20] F. Persson, A. Eliasson, P. Jönsson, Prediction of particle size for water atomised metal powders: parameter study, Powder metallurgy 55 (1) (2012) 45–53. doi:10.1179/1743290111Y.0000000016.

[21] N. Dhokey, M. Walunj, U. Chaudhari, Influence of water pressure and apex angle on prediction of particle size for atomization of copper powder, Advanced Powder Technology 25 (2) (2014) 795–800. doi:10.1016/j.apt.2013.11.014.

[22] M. Pasupathy, J. Martín, A. Rivas, I. Iturriza, F. Castro, Effect of the solidification time on the median particle size of powders produced by water atomisation, Powder Metallurgy 59 (2) (2016) 128–141. doi:10.1080/00325899.2015.1117693.

[23] S. Yenwiset, T. Yenwiset, Effect of the molten metal stream's shape on particle size distribution of water atomized metal powder, Engineering Journal 20 (1) (2016) 187–196. doi:10.4186/ej.2016.20.1.187.

[24] A. Asgarian, Z. Tang, M. Bussmann, K. Chattopadhyay, Water atomisation of metal powders: effect of water spray configuration, Powder Metallurgy 63 (4) (2020) 288–299. doi:10.1080/00325899.2020.1802558.

[25] A. Asgarian, R. Morales, M. Bussmann, K. Chattopadhyay, Water atomisation of molten metals: a mathematical model for a water spray, Powder Metallurgy (2021) 1–19doi:10.1080/00325899.2021.1949801.

[26] F. Persson, N. Hulme, C, G. Jönsson, P, Particle morphology of water atomised iron-carbon powders, Powder Technology 397 (2022) 116993. doi:10.1016/j.powtec.2021.11.037.

[27] V. A. Beck, N. N. Watkins, A. S. Ashby, A. A. Martin, P. H. Paul, J. R. Jeffries, A. J. Pascall, A combined numerical and experimental study to elucidate primary breakup dynamics in liquid metal droplet-on-demand printing, Physics of Fluids 32 (11) (2020) 112020. doi:10.1063/5.0029438.

[28] N. N. Watkins, E. S. Elton, P. H. Paul, V. A. Beck, J. R. Jeffries, A. J. Pascall, Experimentally probing the extremes of droplet-on-demand printability via liquid metals, Physics of Fluids 33 (12) (2021) 121708. doi:10.1063/5.0076594.

[29] W. Hikita, T. Ichimura, C. Inoue, M. Nakaseko, Visualization and modeling for water atomization of low melting point alloy, Advanced Powder Technology 32 (11) (2021) 4235–4244. doi:10.1016/j.apt.2021.09.030.

[30] C. A. Schneider, W. S. Rasband, K. W. Eliceiri, Nih image to imagej: 25 years of image analysis, Nature methods 9 (7) (2012) 671–675. doi:10.1038/nmeth.2089.

[31] E. Villermaux, P. Marmottant, J. Duplat, Ligament-mediated spray formation, Physical Review Letters 92 (2004) 074501. doi:10.1103/PhysRevLett.92.074501.

[32] E. Villermaux, Fragmentation versus cohesion, Journal of Fluid Mechanics 898 (2020). doi:10.1017/jfm.2020.366.

[33] D. Sivakumar, C. Tropea, Splashing impact of a spray onto a liquid film, Physics of fluids 14 (12) (2002) L85–L88. doi:10.1063/1.1521418.

[34] I. V. Roisman, T. Gambaryan-Roisman, O. Kyriopoulos, P. Stephan, C. Tropea, Breakup and atomization of a stretching crown, Physical Review E 76 (2) (2007) 026302. doi:10.1103/PhysRevE.76.026302.

[35] C. Inoue, Y. Izato, A. Miyake, E. Villermaux, Direct self-sustained fragmentation cascade of reactive droplets, Physical review letters 118 (7) (2017) 074502. doi:10.1103/PhysRevLett.118.074502.

[36] D. C. Blanchard, The electrification of the atmosphere by particles from bubbles in the sea, Progress in oceanography 1 (1963) 73–202. doi:10.1016/0079-6611(63)90004-1.

[37] M. Abdelwahed, S. Bengtsson, R. Casati, A. Larsson, S. Petrella, M. Vedani, Effect of water atomization on properties of type 4130 steel processed by l-pbf, Materials & Design 210 (2021) 110085. doi:10.1016/j.matdes.2021.110085.

[38] O. Nichiporenko, Shaping of powder particles during the atomization of a melt with water, Soviet Powder Metallurgy and Metal Ceramics 15 (9) (1976) 665–669. doi:10.1007/BF01157829.